Force Control With a Novel Robotic Catheterization System Based on Braided Sleeve Grippers

Omar Al-Ahmad, Mouloud Ourak, Johan Vlekken, and Emmanuel Vander Poorten

***Abstract*—The complex, deformable, and dynamic cardiovascular system makes precise control of flexible medical instruments a challenging task. An innovative robot-assisted catheterization system (RACS) based on braided sleeves was thus developed to aid interventionalists during cardiovascular procedures. The RACS allows navigating instruments through the vasculature with continuous uninterrupted motion. The complete design and characterization of the developed RACS are presented and experimentally evaluated. The RACS' capability to track dynamic motion is demonstrated. Hereto, heart motion is estimated and fed into a dedicated motion controller. It is further demonstrated that tissue tracking performance can be improved by compensating for hysteresis present along the instrument's length and incorporating a rate-dependent Bouc-Wen model in the motion control strategy. Here, a practical method based on multi-core FBG-inscribed fiber technology is presented for continuous instrument pose tracking. A velocity controller is cascaded with a force control loop to enable instrument tip contact force tracking. An experimental comparison between three different force control strategies was carried out on a benchtop laboratory setup resembling a dynamically moving heart wall. Results confirmed the superior performance of the cascaded force-velocity controller with Bouc-Wen hysteresis compensation. Finally, the RACS system was validated through in-vivo experiments on a living swine which demonstrated its ability to successfully navigate instruments toward the heart.**

***Index Terms*—robot-assisted catheterization system, cardiovascular robots, sleeve-based gripper, hysteresis compensation, FBG multi-core fiber, pose tracking, force control.**

I. Introduction

A. Medical Overview

THE World Health Organization (WHO) reports that cardiovascular diseases (CVDs) are the leading cause of death worldwide. In 2019, they accounted for over 17.9 million deaths globally [1]. With the growing number of individuals affected by CVDs came an increased interest to offer safe and reliable treatments. To reduce perioperative risks, minimally invasive surgery (MIS) approaches were increasingly investigated. In minimally invasive CVD treatment, interventionalists typically employ a class of flexible instruments to navigate the vasculature towards a targeted region of interest [2]. For example, in ablation procedures, cardiologists steer a catheter towards the heart to ablate cardiac tissue. In order to ensure successful scarring of the tissue and reduce perioperative risks, cardiologists must apply a given contact force on the beating heart. In the treatment of Atrial Fibrillation (AFib), the contact force is suggested to remain within a range of $0.1-0.4$ N during ablation [3]. Lower forces could lead to insufficient ablation, while higher forces could puncture the heart wall. Since the catheter undergoes friction with force levels that are an order of magnitude larger than the aforementioned range [4], e.g. at the access port and over the distributed contact with the vessel wall, establishing this low target contact force against a beating heart with poor force feedback is considered an extremely challenging task.

O. Al-Ahmad, M. Ourak, and E. Vander Poorten are with the Department of Mechanical Engineering, KU Leuven University, Belgium (e-mail: first-name.lastname@kuleuven.be)

O. Al-Ahmad and J. Vlekken are with FBGS International, Geel, Belgium (e-mail: oalahmad@fbgs.com, jvlekken@fbgs.com)

B. Robot-Assisted Catheterization Systems

Robot-assisted catheterization systems (RACSs) have been developed to simplify and improve catheter steering and navigation. They are claimed to improve instrument stability, positional precision, and manual control over tissue contact [5]. Studies report their ability to potentially offer more ergonomic, radioactive-free, and precise treatments [6]. Systems like the Sensei® X from Auris Health (Redwood city, CA, USA) demonstrated shortened learning curves and reductions in procedural, ablation and fluoroscopy times [7].

From a mechanical viewpoint, RACSs can be classified based on the employed actuation mechanism to drive the instrument. Note that *instrument* in this context primarily refers to catheters and guidewires. The actuation mechanisms are generally based on: *(1)* rollers, *(2)* belts, *(3)* magnetics, or *(4)* grippers. The first class of actuation employs friction rollers that are pressed upon each other merely allowing for an instrument to pass through. When rotating the rollers, the contact friction between the instrument and rollers serves as the propulsion driving force. Rotation of the instrument is achieved by rotating the complete roller system. The CorPath® GRX from Siemens Healthineers (Erlangen, Germany) makes use of this actuation principle. Belt-based systems enclose an instrument between two parallel belts. When driving the belts, the friction force between the instrument and the belts propels the instrument forwards or retracts it backwards. Instrument rotation can be achieved by moving the belts sideways in opposite directions. The Magellan™ from Auris Health (Redwood city, CA, USA) makes use of this driving principle. An advantage of roller and belt systems is their infinite stroke allowing continuous motion over the instrument's length.

Magnetically actuated systems steer dedicated instruments using large magnets placed externally outside the patient's body. The instrument tip contains magnetic material that aligns with the externally generated magnetic field. The Niobe® ES from Stereotaxis (St. Louis, MO, USA) and the CGCI from Magnetecs (Inglewood, CA, USA) are commercial systems that employ this actuation principle. The final class of actuation relies on grippers to grip or clamp the instrument,

TABLE I
SUMMARY OF RACSS IN THE LITERATURE (DOF = DEGREES OF FREEDOM, MRI = COMPATIBILITY FOR MAGNETIC RESONANCE IMAGING).

Author(s)	Application(s)	DoF	Driving mechanism(s)	Notes on driving mechanism(s)	MRI	Main benefit(s)	Limitation(s)
Bian *et al.* [13]	Vascular interventional surgery	2 for 1 catheter	angular rotation	friction rollers; differential roller-based rotation	No	compact size; force feedback	vulnerability to slip or damage; limited rotation
Wang, Xiao *et al.* [14], [15]	Ileus treatment; Vascular interventional surgery	2 for 1 catheter	angular rotation	friction rollers; gear-based rotation	No	unlimited stroke; force feedback	large size; vulnerability to slip or damage
Fu *et al.* [16]	Electrophysiological catheterization	3 for 1 catheter	angular rotation; tensioned sleeve	friction rollers; gear-based rotation; sliding sleeve	No	unlimited stroke; force feedback	large size; vulnerability to slip or damage
Faddis *et al.* [17]	Electrophysiological catheterization	1 for 1 catheter	magnetism	magnetic guidance system	No	non-contact drive;	large size; low bandwidth
Ma, Song, Guo *et al.* [18]–[20]	(Endo)Vascular interventional surgery	2 for 1 catheter	gripping; linear translation; angular rotation	linear rail gear-based rotation	No	force feedback	large size; limited stroke
Zhang *et al.* [21]	Endovascular catheterization	2 for 1 catheter	gripping; linear translation; angular rotation	conical clamping; linear rail; gear-based rotation	No	force feedback	large size; limited stroke
Omisore *et al.* [22]	Intravascular catheterization	2 for 1 catheter	gripping; linear translation; angular rotation	linear slotted clamps; belt system; gear-based rotation	No	force feedback	large size; coupled DoF
Ganji, Park, Cercenelli, Norouzi-Ghazbi *et al.* [23]–[26]	Electrophysiological catheterization	3 for 1 catheter	gripping; linear translation; angular rotation	dedicated instrument mount; linear rail; gear-based rotation	No	advanced control; improved precision; force feedback	large size; limited stroke
Wang, Lee, Dong *et al.* [27]–[29]	Electrophysiological catheterization	3 for 1 catheter	gripping; linear translation; angular rotation	dedicated instrument mount; linear rail; gear-based rotation; fluidic actuation	Yes	advanced control	large size; limited stroke
Bao *et al.* [30], [31]	Vascular interventional surgery	2 for 1 catheter; 2 for 1 guidewire	gripping; linear translation; angular rotation	conical clamping; linear rail; gear-based rotation	No	multiple instrument drive; force feedback	diameter specific grippers; large size; limited stroke
Xiang *et al.* [32]	Cardiovascular intervention	2 for 1 catheter; 2 for 1 guidewire	gripping; linear translation; angular rotation	linear rail; gear-based rotation	No	multiple instrument drive; force feedback	large size; limited stroke
Abdelaziz *et al.* [33]	Endovascular catheterization	2 for 1 catheter; 2 for 1 guidewire	gripping; linear translation; angular rotation	linear rail; gear-based rotation fluidic actuation	Yes	quick release; force feedback	large size; limited stroke
Wang, Lu *et al.* [34], [35]	Endovascular catheterization	4 for 2 catheters 4 for 2 guidewires	gripping; linear translation; angular rotation	linear slotted clamps; linear rail; gear-based rotation	No	multiple instrument drive; generic instrument grippers	large size; limited stroke
Srimathveeravalli *et al.* [36]	Endovascular catheterization	3 for 1 catheter 2 for 1 guidewire	gripping; linear translation; angular rotation	friction rollers; linear rail; gear-based rotation	No	multiple instrument drive; force feedback	large size; limited stroke
Al-Ahmad *et al.* (proposed device)	(Endo-) Cardiovascular catheterization	2 for 1 instrument (catheter or guidewire)	gripping; linear translation; angular rotation	sleeve-based grippers; linear rail; gear-based rotation	No	distributed gripping; modular grippers; force control	single instrument control (catheter or guidewire)

in combination with translation and rotation mechanisms to propel and rotate the gripper. A limitation of these systems is that they usually have a limited stroke and may require regripping. Table I provides an overview of a variety of different RACSs developed in the literature. The reader is referred to [8], [9] for a broad review of such systems.

Common shortcomings of RACSs include improper instrument support and handling [10], [11]. This leads to discontinued manipulation and implies that manual interventions are often necessary to realign or reinstall the instrument within the RACS. Frictional forces often prevent translation of force towards the instrument tip [12]. Accordingly, conventional RACS tend to apply a large gripping force on the instrument body to be able to thrust the instrument against friction while preventing it from slipping. Unfortunately, large pressure concentrations may cause local damage to the instrument leading to increased buckling and instability. Furthermore, RACSs are generally designed for precise instrument steering and navigation [5], but are not suited for tissue motion or contact force tracking.

C. Paper Objectives and Contributions

This work introduces the design and experimental validation of a new RACS exploiting a braided sleeve gripper mechanism to drive medical instruments. The novel sleeve-based gripper generates a large *distributed* gripping force along the instrument body to avoid instrument slip and prevent potentially destructive local forces, in contrast to other gripper-based mechanisms. By using a pair of sleeve-based grippers and a precise regripping strategy, continuous infinite-stroke instrument motion is achieved. Rotation of the instrument about its longitudinal axis is done by rotating the gripper assembly about the axisymmetric sleeve axis. The RACS can thus drive instruments with two independent degrees of freedom (DoF): translation along, and rotation about the longitudinal axis.

Our previous work on local one-dimensional heart motion estimation based on a multi-core fiber (MCF) with inscribed fiber Bragg gratings (FBGs) [37] is combined with the RACS development to enable dynamic tissue tracking. The work is expanded to obtain a practical method for real-time instrument tip pose tracking to be employed for hysteresis identification and compensation within robotic catheterization procedures. The hysteresis compensated motion trajectory is then fed to a velocity controller. As a further step, the velocity controller is subsequently closed with a force control loop to achieve dynamic tissue contact force tracking. This makes it possible to precisely follow the dynamic tissue motion while maintaining a constant desired contact force at the instrument tip.

According to the above, the contributions of this paper are summarized as follows:

1) Development and experimental evaluation of a novel sleeve-based RACS to deploy generic instruments in two DoF with no slip and high reliability.
2) Introduction of a novel method based on FBG-MCFs for instrument tip tracking to enable online hysteresis identification and compensation within robotic catheterization procedures. This is carried out to achieve effective instrument tip tissue motion and contact force tracking.
3) Experimental validation of the proposed RACS on a live swine in a catheterization laboratory (CathLab).

The remainder of this paper is structured as follows: Section II outlines the system requirements and describes the overall RACS design. Section III provides the experimental characterization and evaluation of the proposed RACS. Section IV discusses aspects regarding tissue motion tracking and introduces a practical method for instrument tip pose tracking using FBG-inscribed MCFs within a robotic catheterization context. Section V expands on this idea and incorporates a force control loop to obtain dynamic tissue contact force tracking. The experimental validation of the RACS' instrument deployment capability on a live swine is presented and discussed in

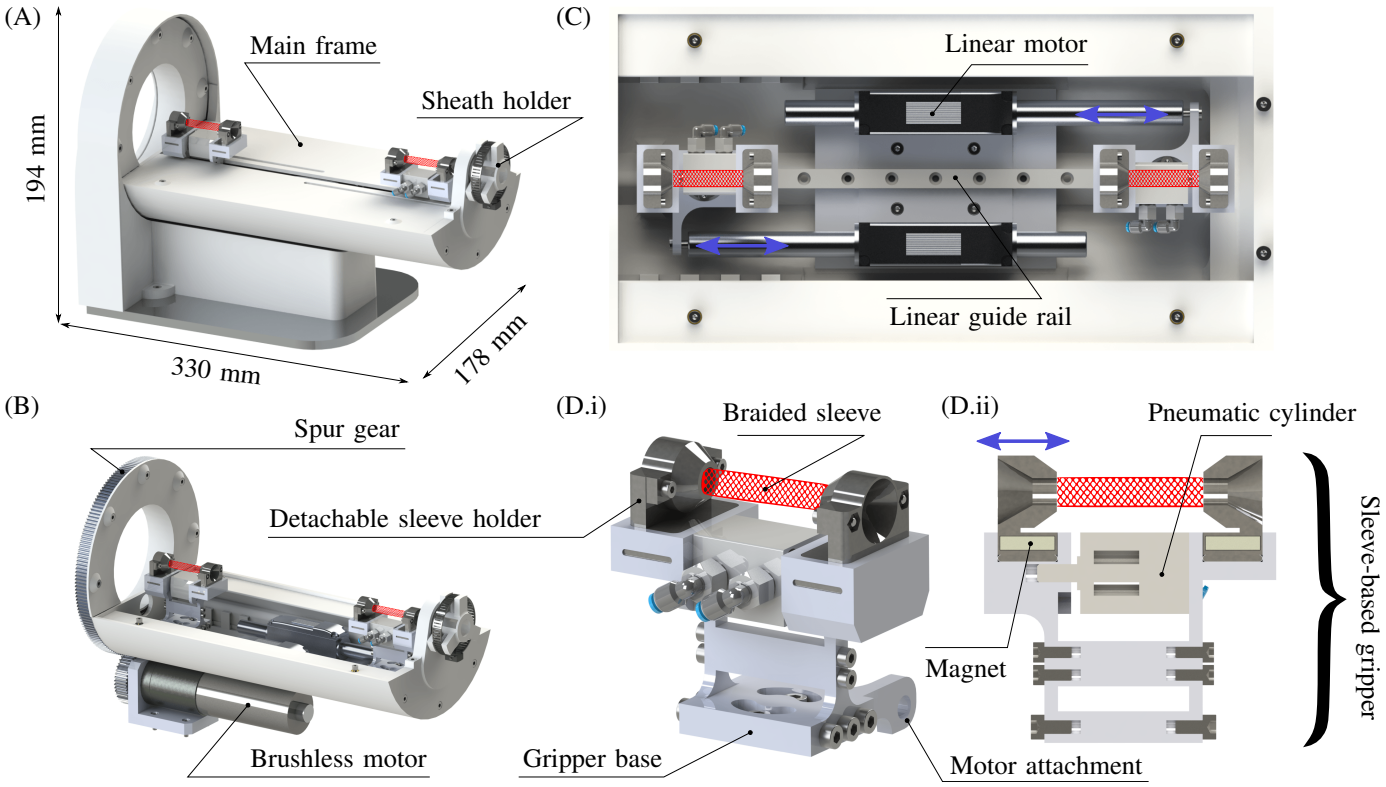

Fig. 1. Illustration of the: **(A)** isometric view of the complete RACS, **(B)** isometric view of the RACS without the enclosing frames, **(C)** top view of the RACS without the enclosing frames nor the spur gears, **(D.i)** isometric view of the sleeve-based gripper, **(D.ii)** sectional side view of the sleeve-based gripper.

Section VI. Finally, Section VII provides a discussion and conclusion of the results and offers an outlook for future work.

II. System Overview

A. System Requirements

The developed RACS was designed to drive generic instruments via teleoperation for catheterization procedures. Accordingly, the following design requirements were set forward:

a) instrument control with two bidirectional DoF: translation and rotation about the instrument's longitudinal axis;
b) infinite stroke and continuous instrument motion, with continuous insertion speeds up to 40 mm/s;
c) prevention of excessive local stress concentrations when gripping and avoidance of instrument slip;
d) a minimum linear gripping force of ≥ 4.5 N, and a rotational gripping torque of ≥ 15 Nmm [38]–[40], to meet practical clinical requirements;
e) effective heart motion tracking while maintaining a constant contact force in the range of $0.1 - 0.4$ N [3];

B. System Description

1) Overall system: An illustration of the proposed RACS is provided in Fig. 1. The RACS comprises a 3D printed ABS main frame to support all driving elements. An aluminium plate mounted on the ABS main frame provides stiffness and holds the driving elements together. Two LM 2070-080-11 linear DC-servomotors (Faulhaber, Schonaich, Germany) are mounted on both sides of the aluminium plate. A linear guide rail is fixed on the plate between the linear motors. A pair of sleeve-based grippers (Fig. 1D) are mounted on separate linear blocks. These are in turn mounted on the linear guide rail (Fig. 1C). The gripper base is attached to the linear motors such that any motion created by the motors is directly translated to the sleeve-based grippers. From the back end, a PRT-04-100-TO-ST spur gear system (IGUS, Koln, Germany) is used for the rotational DoF. The pinion is attached to a EC-i 40 130W high torque brushless EC motor (maxon group, Sachseln, Switzerland), while the gear is attached to the main frame. The spur gear arrangement allows the complete system to freely rotate about the instrument's longitudinal axis.

2) Sleeve-based grippers: The principal component of the novel gripping mechanism is a stretchable braided sleeve. The idea behind this new gripper is that the sleeve gradually changes its diameter when it is longitudinally extended or retracted. This allows for altering the grip upon an instrument which is centrally introduced inside the sleeve. When the sleeve is fully extended, it is able to apply a firm distributed grip upon the instrument. The contact between the sleeve and the instrument acts along the entire sleeve's length. This results in a large friction force that is used to transmit the propulsion force delivered by the linear motors to the instrument's body. The *distributed* compression force normal to the instrument's surface avoids local stress concentrations. The braided sleeve is attached to two sleeve holders on either side (Fig. 1D). Each sleeve holder is comprised of two parts that contain conical profiles which are able to fit on top of each other. During assembly, the ends of the braided sleeve are expanded, by

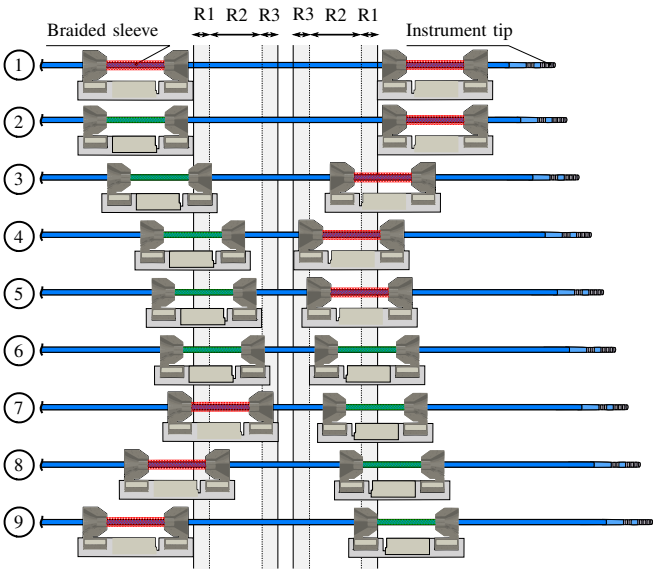

Fig. 2. Illustration of the dynamic regripping strategy for instrument translation with continuous motion. The gripper with the red sleeve shows the sleeve in a relaxed state, i.e. the instrument is released. The gripper with the green sleeve shows the sleeve in an extended state, i.e. the instrument is gripped.

unwinding the braid, and fitted between the conical profiles of the sleeve holder. The two sleeve holder parts are then compressed upon each other to rigidly hold the sleeve. Note that the diameter of the braided sleeve is smaller than the inner diameter of the conical part of the sleeve holders. The sleeve holders are then inserted into dedicated slots within a gripper block and firmly locked in position using permanent magnets. The magnets are strong enough to lock the detachable sleeve holders in place while being weak enough for a user to pull them out. This allows rapid replacement of the grippers and the instrument onto the RACS. One part of the sleeve holders is fixed at one side, while the other can freely translate back and forth using an ADVC-10-10-A-P pneumatic cylinder (FESTO, Esslingen, Germany) placed between both sleeve holders. Apart from being lightweight, this pneumatic actuator is very fast allowing rapid gripping or releasing of the instrument. When the sleeve is extended, the motion of the linear motor is transferred $1:1$ to the instrument. Conversely, when the sleeve is relaxed, the motion of the linear motor has negligible effect on the position of the instrument. It is important to note that the braided sleeve concept allows for the use of generic types of instruments with varying diameters. Different sleeves with varying diameters can be easily prepared and exchanged.

C. Continuous Motion Through Dynamic Regripping

Continuous instrument motion through the vasculature allows for rapid deployment and uninterrupted control over the instrument's position. Achieving this using a gripper-based mechanism involves use of a pair of grippers and a precisely synchronized regripping strategy. This is in contrast to an embodiment comprising a single gripper which would require regripping and repetitive gripper homing at the end of its stroke. The continuous regripping strategy employed in the proposed RACS involves ⑨ steps that are schematically illustrated in Fig. 2. The method is based on precisely controlling the linear motions of the grippers and corresponding changes in their gripping/releasing states. The total stroke of each gripper is divided into three consecutive regions such that R1 is the region at the beginning of the stroke, R2 is the central region, and R3 is the region at the end of the stroke. The order of these regions is opposite for both grippers. The gripping strategy is then as follows: ① Both grippers begin at their home position, i.e. at the start of range R1. ② The instrument is gripped by extending the integrated pneumatic cylinder in the left hand side (LHS) gripper. The instrument at the right hand side (RHS) gripper remains released. ③ The LHS gripper moves forward at a designated velocity V, while the RHS gripper moves backward at a velocity $V \cdot \alpha$ where $\alpha > 1$. This is to ensure that the RHS gripper can reach the end of it stroke before the LHS reaches the end of its stroke. ④ The RHS gripper reaches the end of its stroke, stops, and waits for the LHS gripper to reach the start of range R3. ⑤ The LHS gripper reaches the start of range R3. Now, the RHS gripper moves forward with a velocity V, similar to the LHS gripper. ⑥ When the LHS gripper reaches halfway along range R3, the RHS gripper extends the pneumatic cylinder and grips the instrument. Now, both grippers have a firm grip on the instrument and move at velocity V. ⑦ Just before the LHS gripper reaches the end of its stroke, it releases the instrument. ⑧ The LHS gripper reaches the end of its stroke and moves backwards with velocity $V \cdot \alpha$. ⑨ The LHS gripper reaches the home position and waits for the RHS gripper to reach the start of range R1. The process is then repeated with the lead of the second gripper, and consequently repeated until the desired position is reached. The sequence outlined from steps ① to ⑨, and especially steps ⑤ to ⑦, are termed *dynamic regripping*, as the instrument is gripped/released during motion. The reader is also referred to the work of Lee *et al.* [41] for the description of a similar motion strategy.

III. Fundamental RACS Evaluation

Figure 3 provides an illustration of the developed RACS and the corresponding experimental setups employed for its evaluation and characterization. These fundamental experiments are discussed in the following.

A. Linear Gripping Force

Figure 3C illustrates the experimental setup for the characterization of the linear gripping force of the sleeve-based grippers. Experiments were carried out on a commercial 0.9 mm diameter HydroSteer™ guidewire (Abbott, IL, United States) and an 8 Fr Thermocool SmartTouch® ablation catheter (Biosense Webster, CA, United States). For a given experiment, the instrument was inserted into its dedicated grippers and mounted onto the RACS. Figures 3A and 3B depict the different grippers for the catheter and guidewire, respectively. A thin steel cable was rigidly attached to the tip of the instrument using adhesives, routed around a pulley, and attached to a light cardboard box with added weights on the opposite end. To characterize the linear gripping force for a *single* gripper,

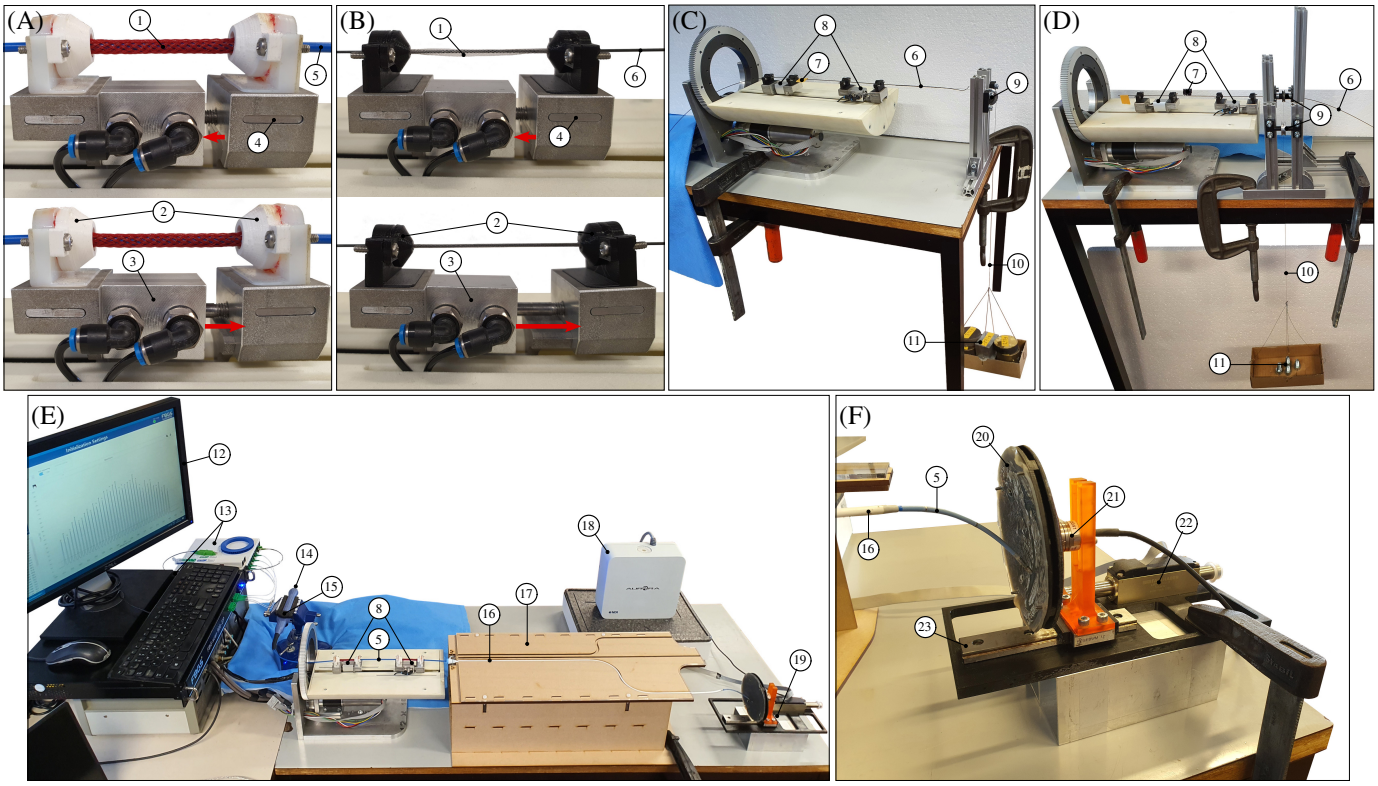

Fig. 3. Illustration of the different experimental setups: sleeve-based gripping with released (top) and gripped (bottom) states of a **(A)** catheter and **(B)** guidewire, **(C)** identification of translational gripping force, **(D)** identification of rotational gripping force, **(E)** characterization of translation and rotation behaviour, identification and compensation of linear hysteresis, and catheter contact force tracking, **(F)** detailed view of the catheter contact force tracking setup. The experimental setups are comprised of the following components: ① 3.18 mm diameter Flexo® polyethylene terephthalate braided sleeve (Techflex, NJ, USA) for the catheter and 0.4 mm diameter polyester braided sleeve (Bossert und Kast, Pforzheim, Germany) for the guidewire, ② 3D-printed sleeve holders, ③ pneumatic cylinder, ④ steel plate, ⑤ catheter, ⑥ guidewire, ⑦ tape cut-out, ⑧ sleeve-based grippers, ⑨ pulley, ⑩ steel cable, ⑪ weights, ⑫ monitor for wavelengths display, ⑬ FBG-Scan 908-EP optical interrogator and fanout (FBGS International NV, Geel, Belgium), ⑭ FBG-inscribed MCF (FBGS International NV, Geel, Belgium), ⑮ catheter handle, ⑯ guiding sheath, ⑰ MDF cut-out with slotted paths for sheath insertion, ⑱ electromagnetic tracking system, ⑲ catheter force tracking setup, ⑳ Eco-Flex silicon layer with thin gel surface, ㉑ Nano17 6-axis force sensor (ATI Industrial Automation, NC, United States), ㉒ LM 2070-080-11 linear servomotor (Faulhaber, Schonaich, Germany), and ㉓ linear guide.

the gripper was fully extended using the pneumatic cylinder at a pressure of 6 bars, which corresponds to a linear extension force of 47 N. Weights were gradually and incrementally added into the cardboard box until a slight motion of the instrument was observed. A tape cut-out was attached to the instrument to make this visualization more clear. Note that by design, the extension direction of the grippers is opposite. This means that for the first gripper, added weights would cause it to extend further, while for the second gripper, added weights would cause it to retract. This is analogous to a compressive or tensile load on the grippers. Accordingly, the experiment was repeated 4 times per instrument and per gripper. The mean linear gripping force for the first gripper enclosing the catheter and guidewire was 21.8 N and 24.9 N respectively, and 17.3 N and 19.7 N for the second gripper. The results clearly show that minimum gripping forces, both for the catheter and guidewire, are much larger than the minimum requirement of 4.5 N.

B. Rotational Gripping Torque

Figure 3D illustrates the experimental setup for the characterization of the rotational gripping torque of the sleeve-based grippers. The experiment methodology is similar to the one carried out for the characterization of the linear gripping force. Here, the instrument is inserted and rigidly fixed into a pulley using adhesives. Weights added into the cardboard box causes a rotation of the pulley, and thus a torque onto the instrument. Again, the experiment was repeated 4 times per instrument. The mean rotational gripping torque for the grippers enclosing the catheter and guidewire was 38.5 Nmm and 16.7 Nmm, respectively. The results show that the gripping torque, for both the catheter and guidewire, is larger than the minimum requirement of 15 Nmm. Note, however, that this requirement is predominantly targeted at larger diameter instruments, i.e. catheters. Smaller diameter guidewires are generally subjected to lower resistive torques during navigation or manipulation.

C. Continuous Motion Through Dynamic Regripping

Figure 3E illustrates the experimental setup for the evaluation of the continuous motion dynamic regripping strategy. An 8 Fr Preface® guiding sheath (Biosense Webster, CA, United States) was used to guide the instruments during the experiment. The sheath was placed into a MDF cut-out with a slotted path consisted of a straight segment and two 90^o bends in opposite directions, each with a radius of 50 mm. This was an exaggerated path profile showcasing the RACS' functionality under severe circumstances. An electromagnetic (EM) tracking

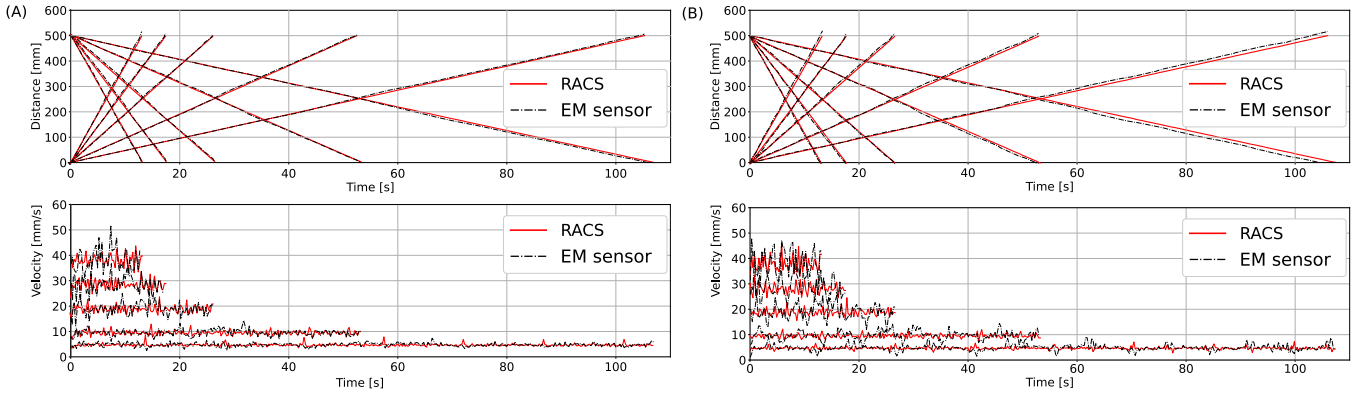

Fig. 4. Example results of the dynamic regripping experiments for a complete translational motion of 500 mm at different velocities: 5 mm/s, 10 mm/s, 20 mm/s, 30 mm/s, and 40 mm/s. **(A)** catheter insertion and retraction, **(B)** guidewire insertion and retraction.

sensor was rigidly fixed to the tip of the instrument using a thin heat shrink with internal adhesive. An Aurora® EM tracking system (Northern Digital, Waterloo, Canada) was used to track the pose of the EM sensor attached to the instrument tip at a rate of 40 Hz. The configuration of the EM tracking system allowed it to have a field of view of just over 500×500 mm. Accordingly, the instrument motion was limited to 500 mm to maintain trackability of the EM sensor for the complete motion trajectory. The stroke of a single gripper was set to be 50 mm, meaning that dynamic regripping occurs at roughly every 50 mm intervals. The experiments were carried out for the following configuration sets: *(1)* catheter and guidewire, *(2)* forward and backward motion, and *(3)* different velocities in the range $5-40$ mm/s. The experiments were repeated 4 times for each configuration combination. The distance travelled by the EM sensor was computed by cumulatively summing the distances between EM positions for consecutive time steps. However, since the EM position data is noisy, cumulatively summing those distances would lead to an inaccurate result. Accordingly, the EM position data was first filtered using an average filter with a window of 16 elements (or 400 ms). The velocity profile was obtained by deriving the EM position profile with respect to time. Position and velocity at the RACS side were obtained through the linear motor's Hall sensors.

Figure 4 illustrates a few example results for the aforementioned experiments. It can be clearly seen that the instruments exhibit a smooth and jerk-free motion for the complete path even though regripping occurs approximately 10 times. This is the case for both motion directions and for the varying motion velocities. The resulting errors between the EM and RACS sensor measurements for all configuration trials are summarized in Table II. It can be seen that for all configurations, motion tracking is sufficiently accurate for both instruments. On average, for the different velocities and motion directions, the maximum tracking error for the catheter and guidewire was found to be 10.9 mm and 15.8 mm, respectively. This corresponds to a maximum tracking error of 2.2 mm and 3.2 mm per 100 mm motion, respectively. Hence, the expected maximum possible tracking error for any given motion trajectory and for any given instrument would be around 3.2% of the total travelled distance. This is an acceptable result given that these deviations occur in an open-loop control scheme. Furthermore, in practical settings *(a)* additional visual feedback is provided to the interventionalist during the procedure via fluoroscopy, and *(b)* the tracking error is smaller for lower velocities especially when intricate small motions are needed where operators automatically lower the commanded velocity levels.

TABLE II
INSTRUMENT MOTION ERRORS GIVEN AS: MEAN ± STANDARD DEVIATION (MAXIMUM). UNITS ARE MM FOR POSITION AND MM/S FOR VELOCITY.

	Catheter				Guidewire			
	Forwards		Backwards		Forwards		Backwards	
Velocity	Position	Velocity	Position	Velocity	Position	Velocity	Position	Velocity
5 mm/s	2.3 ± 2.7 (7.9)	0.1 ± 0.8 (4.1)	3.0 ± 3.0 (8.6)	0.1 ± 0.8 (5.5)	6.9 ± 4.4 (17.0)	0.2 ± 1.1 (6.1)	6.7 ± 5.6 (19.5)	0.2 ± 1.2 (6.6)
10 mm/s	1.2 ± 2.6 (6.9)	0.1 ± 1.3 (6.7)	0.3 ± 2.9 (6.9)	0.1 ± 1.5 (8.4)	2.6 ± 4.1 (12.0)	0.2 ± 1.8 (8.5)	3.6 ± 4.3 (11.1)	0.2 ± 2.0 (8.9)
20 mm/s	0.8 ± 2.6 (7.6)	0.1 ± 2.3 (8.9)	3.3 ± 2.8 (9.5)	0.1 ± 2.5 (12.9)	2.9 ± 4.1 (12.6)	0.4 ± 3.5 (15.3)	2.5 ± 4.5 (15.3)	0.4 ± 4.2 (25.9)
30 mm/s	2.6 ± 3.3 (10.9)	0.5 ± 3.9 (19.1)	4.4 ± 3.2 (11.0)	0.1 ± 4.1 (19.7)	0.5 ± 4.9 (17.2)	1.0 ± 6.6 (34.6)	4.5 ± 4.5 (12.2)	0.4 ± 4.7 (14.2)
40 mm/s	4.4 ± 6.5 (26.1)	1.6 ± 6.8 (36.6)	0.8 ± 4.5 (13.9)	1.4 ± 7.9 (47.4)	4.7 ± 7.2 (30.6)	2.4 ± 9.3 (52.5)	2.9 ± 4.1 (10.5)	0.7 ± 5.6 (15.3)

D. Dynamic Instrument Rotation

The experimental setup in Fig. 3E was used for the characterization of the instrument's dynamic rotation behaviour. The instrument was first navigated all the way until the tip was slightly protruding out of the enclosing sheath. Note that one would expect this to be the worst case scenario as the friction acting on the instrument body is maximal. An EM tracking sensor was again rigidly attached to the instrument tip. The effect of the attachment of the EM sensor to the instrument tip is considered to be negligible since the instrument was found to be reasonably stiff and since the EM sensor was very small in size and weight. The experiment involved rotating the instrument using the RACS for two complete revolutions in a clockwise direction and then back with two complete revolutions in a counter-clockwise direction. These rotational cycles were repeated 4 times for varying rotational velocities in the range $14.4 - 72.0$ deg/s. To mitigate noise effects, the EM pose data was filtered using an average filter with a window of 16 elements (or 400 ms). The EM sensor's $z-$axis which is directed along the sensor's longitudinal axis, was

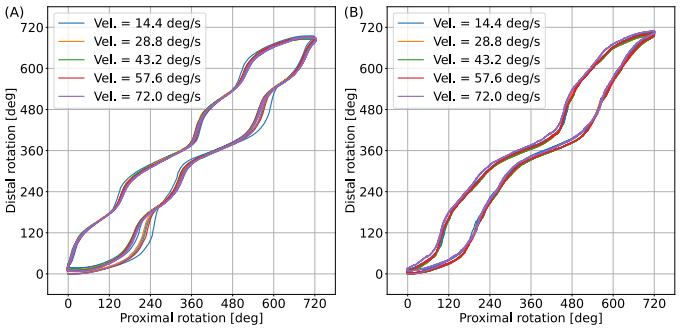

Fig. 5. Results of the dynamic rotation experiments. **(A)** catheter rotation, **(B)** guidewire rotation.

placed parallel to the longitudinal axis of the instrument tip. Accordingly, the angular displacement of the EM sensor was computed as the change in angle about its $z-$axis. This angular displacement was cumulatively summed between consecutive time steps to obtain the total displacement with respect to the initial reference.

The results of the dynamic instrument rotation experiments are depicted in Fig. 5. A clear hysteric behaviour can be observed when comparing the proximal rotation of the instrument at the RACS side with the distal rotation at the instrument tip. This is an expected behaviour [42], [43] due to the presence of friction and play between the instrument and the guiding sheath, and the elastic rotational energy stored in the instrument due to its compliant nature. Although hysteresis is present, it can be seen that after two complete cycles, both catheter and guidewire rotation almost match the rotation of the RACS. The error in rotation angle is around 25 deg, or 3.5% of the total rotation. This indicates a minimal slippage between the sleeve-based grippers and the embedded instrument. Finally, a high repeatability of the rotational behaviour independent of the velocity can also be observed. If high precision rotation would be necessary, the hysteresis behaviour could be modelled and compensated.

IV. Dynamic Tissue Motion Tracking

Tissue motion tracking typically involves estimation of the tissue's motion profile and feeding it to a position/velocity controller. However, as previously discussed, there is often a notable hysteric behaviour present between the instrument motion at the tip and where it is being driven at the proximal end. To improve tissue tracking performance, the hysteresis behaviour is often first modelled, and subsequently compensated in the position/velocity controller [42]–[44]. Loschak *et al.* demonstrated in-vivo tissue tracking by modelling robot kinematics and tissue motion coupled with predictive filtering [45]. The approach, however, was based on ultrasound guidance and therefore required ultrasound measurements. Yu *et al.* followed a different approach where they made use of nonlinear control theory to propose a motion tracking controller with actuator input constraints, unknown initial conditions, and unknown robot dynamics [46]. Their adaptive impedance controller was shown to enable smooth control and safe interaction between the robot and its environment. On the other hand, there exist alternative approaches that make use of machine-learning based methods that can be coupled with the instrument's kinematics model to compensate and control its linear and bending motions [47], [48]. In this paper, an approach based on tissue motion estimation and tracking is employed. The following sections discuss relevant aspects related to this topic.

A. Local Heart Motion Estimation

The topic of heart motion estimation has been abundantly tackled in literature. The majority of techniques employed for this task primarily rely on imaging modalities. These may include: fluoroscopy [49], ultrasound [50], computed tomography (CT) [51], camera vision [52], or ECG-gated magnetic resonance (MR) [53]. While the underlying techniques and algorithms may differ between the aforementioned imaging modalities, the general work-flow is similar. On the other hand, our previous work [37] focused on achieving similar results following a different methodology. The work was concerned with local one-dimensional heart motion estimation based on FBG-inscribed MCFs. The method involves reconstructing the instrument's 3D shape in real-time [54], [55], and tracking its position over a few cardiac cycles. This information is used to estimate the local heart motion direction vector to project the 3D tip points. Coupled with an unscented Kalman filter (UKF), a temporal quasi-periodic estimation of the heart motion profile is obtained. For brevity, only an overview of the method was provided here. The reader is referred to our previous work for a detailed description [37]. The estimated heart motion, presented in our previous work, would serve as the motion controller's feedforward signal.

B. Bouc-Wen Hysteresis Modelling and Compensation

Since the amount of viscous friction present between the instrument and the sheath varies with velocity, and heart motion frequency may vary with time, a rate-dependant Bouc-Wen hysteresis model was employed in this work for hysteresis modelling and compensation purposes. Considering that x_{in} is the position of the instrument at the proximal RACS side, and that x_{out} is the position of the instrument tip, the Bouc-Wen model representation of the hysteric behaviour between x_{in} and x_{out} is given as follows [56], [57]:

$$x_{out}(t) = \alpha_x x_{in}(t) - h(t, \dot{x}_{in}), \tag{1}$$

$$\dot{h}(t, \dot{x}_{in}) = \alpha \dot{x}_{in}(t) - \beta |\dot{x}_{in}(t)| h(t, \dot{x}_{in}) |h(t, \dot{x}_{in})|^{\gamma-1} - \delta \dot{x}_{in}(t) |h(t, \dot{x}_{in})|^{\gamma}, \tag{2}$$

where $h(t, \dot{x}_{in})$ is the state variable, $\dot{h}(t, \dot{x}_{in})$ is the derivative of the state variable with respect to time t, and $\dot{x}_{in}$ is the derivative of the proximal instrument position with respect to time. α_x, α, β, δ, and γ are Bouc-Wen model constants, and $|\square|$ is the absolute value operator.

The experimental setup shown in Fig. 3E was used to characterize the hysteric relationship between the input and output positions, x_{in} and x_{out}, and to obtain an estimation of the Bouc-Wen model parameters α_x, α, β, δ, and γ. At the

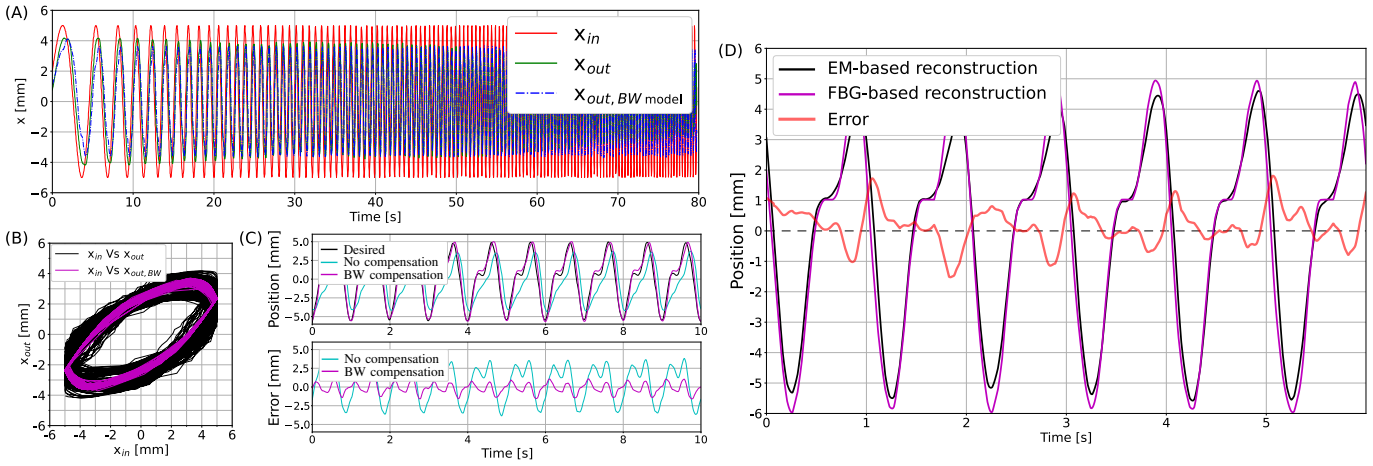

Fig. 6. Results of the hysteresis identification and compensation experiments. **(A)** variable-frequency input signal x_{in} at the instrument's proximal side and the corresponding output x_{out} at the instrument's distal side, including the Bouc-Wen model output $x_{out,BW\,model}$, **(B)** measured input signal x_{in} versus output signal x_{out} including the Bouc-Wen model estimation of the hysteric profile $x_{out,BW}$, **(C)** comparison of the instrument tip position profile with and without Bouc-Wen hysteresis compensation, **(D)** comparison of the instrument tip position profile based on EM and FBG based reconstructions.

proximal side of the RACS, the gripper was commanded to move at a varying frequency sinusoidal signal, representing $x_{in}(t)$, which is in the form:

$$x_{in}(t) = A \sin\left(2\pi \int \left(f_s + \frac{f_f - f_s}{t_{tot}}\right) dt\right), \qquad (3)$$

where $A = 5$ mm is the sine amplitude, $f_s = 0.1$ Hz and $f_f = 3.0$ Hz are the starting and final frequencies, $t_{tot} = 80$ s is the total time, and $dt = 0.025$ s is the sampling time. A varying frequency sinusoidal signal was employed to encompass a wide range of velocities and to capture the hysteresis rate-dependency effects. At the distal end, an EM sensor was attached to the tip of the instrument to measure its real-time 3D position. The instrument tip was made to slightly protrude out of the surrounding sheath. The tip motion is thus considered to be one-dimensional throughout the sinusoidal motion. A straight 3D line can thus be fitted through the 3D tip positions, which are then projected onto this line to obtain a 1D temporal profile representing $x_{out}(t)$. Bouc-Wen model constants are obtained through a non-linear least-squares optimization to fit equations (1) and (2) to the measured data $x_{in}(t)$ and $x_{out}(t)$. The results of identification experiment can be seen in Fig. 6A and Fig. 6B. The Bouc-Wen model parameters were found to be $\alpha_x = 1.91$, $\alpha = 1.57$, $\beta = 0.0132$, $\delta = -0.0055$, and $\gamma = 2.56$. The Bouc-Wen model displays proper fitting of the experimentally measured data and is able to encompass the complete velocity range.

The heart motion profile can be represented as a periodic multi-frequency sinusoid in the following form [58]:

$$x_h(t) = c + \sum_{i=1}^{m} r_i \sin(i\omega t + \theta_i), \qquad (4)$$

where $x_h(t)$ is the position of the heart motion, c is the motion offset, m is the total number of sinusoidal harmonics, r_i is the amplitude of the i^{th} sinusoidal harmonic, ω is the fundamental angular frequency, θ_i is the angular phase shift of the i^{th} sinusoidal harmonic, and t is the time. Yuen *et al.* [58] carried out a spectral analysis of the motions at the mitral valve annulus and found that the major motion components were around 1.3 Hz, 2.6 Hz, and 5.2 Hz, while higher frequency components exhibited a notably decreasing amplitude. This information was used to simulate a heart motion with the following properties: $c = 0.0$ mm, $r_{i=1..8} = [4.0, 2.0, 0.4, 0.1, 0.005, 0.001, 0.0005]$ mm, $\omega = 2\pi$ rad/s, and $\theta_{i=1..8} = [0.0, 2.8, 2.8, 0.0, 3.7, 1.2, 5.6, 7.3]$ rad.

The experimental setup in Fig. 3E was again utilized to evaluate the tracking performance incorporating hysteresis compensation. The results of this experiment are shown in Fig. 6C. A comparison of the motion tracking performance was made with and without hysteresis compensation. For a peak-to-peak (PTP) motion amplitude of around 12 mm, the mean and maximum tracking error without hysteresis compensation was 0.55 ± 2.26 mm and 3.85 mm, respectively. Alternatively, the mean and maximum tracking error with hysteresis compensation was 0.14 ± 0.68 mm and 1.71 mm, respectively. The maximum tracking error thus drops from 32.1% of the PTP amplitude to 14.3%. It is therefore clear that hysteresis compensation is essential and has the potential to significantly improve tissue motion tracking performance. Furthermore, the choice for a rate-dependent Bouc-Wen model appears to be adequate for such purposes.

C. Tip Pose Tracking Using FBG-MCFs

The hysteresis identification and compensation experiments in Section IV.B employed an EM tracking sensor at the tip to reconstruct the one-dimensional tip motion. Practically however, many catheterization instruments do not contain EM tracking sensors. FBG-MCFs on the other hand, are small (diameter $\approx$ 200 microns), and could be easily embedded within the instrument's working channel. A FBG-MCF based method is thus proposed for real-time instrument tip pose tracking, within the context of robotic catheterization procedures, and is explained in what follows.

Consider a 3D curve $\boldsymbol{C}_k$ composed of N discrete coordinates positioned along a discrete arc length s, and having a total arc length l_s. Every coordinate is also defined by a tangent, normal, and binormal (TNB) frame representing its orientation. This curve represents the shape of the instrument [54], [55], at a given time step k. The 3D curve is defined by its curvature $\boldsymbol{\kappa}_k$ and curvature angle $\boldsymbol{\theta}_{\boldsymbol{b},k}$ profiles. We assume a situation where the instrument is embedded within a surrounding sheath exhibiting a quasi-static shape. Now, consider a case where the instrument is translated forwards by a discrete distance ζ at time step $k+1$. Given that the surrounding shape is quasi-static, the curvature profile $\boldsymbol{\kappa}_k$ will simply shift towards the origin of the arc length, i.e. towards $s=0$ at the proximal end of the instrument, by an amount equal to ζ to obtain $\boldsymbol{\kappa}_{k+1}$. In other words, the curvature $\boldsymbol{\kappa}_{k+1}$ between $s=0$ and $s=l_s-\zeta$ would be equal to the curvature $\boldsymbol{\kappa}_k$ between $s=\zeta$ and $s=l_s$. As such, the shapes of the curves $\boldsymbol{C}_k$ and $\boldsymbol{C}_{k+1}$ in the regions between $s=\zeta$ and $s=l_s-\zeta$ would be identical. We will now carry this idea forward and identify a step-wise strategy for tracking the pose of the instrument tip in real-time:

1) Reconstruct the instrument shape and curvature profile for time step k to obtain $\boldsymbol{C}_k$ and $\boldsymbol{\kappa}_k$, and time step $k-1$ to obtain $\boldsymbol{C}_{k-1}$ and $\boldsymbol{\kappa}_{k-1}$;
2) Crop the curvature profile $\boldsymbol{\kappa}_k$ between the arc length $s=\zeta_{max}$ and $s=l_s-\zeta_{max}$ to obtain $\boldsymbol{\kappa}_{k,c}$, where $\zeta_{max}<l_s$ is the maximum expected distance travelled by the instrument between any two given time steps;
3) Shift $\boldsymbol{\kappa}_{k,c}$ along the arc length from s=0 to s=2ζ_{max} with a finite arc length increment ds. For every iteration i, compute the sum of squared differences ϵ_i between the shifted $\boldsymbol{\kappa}_{k,c}$ and the corresponding segment of k_{k-1} for the same arc length interval;
4) Determine the arc length s_{min} where the sum of squared differences ϵ_i is minimal. The signed distance travelled by the instrument will be $\zeta_{max}-s_{min}$;
5) Crop curve $\boldsymbol{C}_{k-1}$ between arc length $s=s_{min}$ and $s=s_{min}+l_s-2\zeta_{max}$ to obtain $\boldsymbol{C}_{k-1,c}$, and curve $\boldsymbol{C}_k$ between $s=\zeta_{max}$ and $s=l_s-\zeta_{max}$ to obtain $\boldsymbol{C}_{k,c}$;
6) Translate curve $\boldsymbol{C}_{k-1,c}$ to the origin by subtracting the coordinate of its first point $\boldsymbol{C}_{k-1,c}(0)$, and curve $\boldsymbol{C}_{k,c}$ to the origin by subtracting the coordinate of its first point $\boldsymbol{C}_{k,c}(0)$. Find the rotation matrix $\boldsymbol{R}$ between $\boldsymbol{C}_{k-1,c}$ and $\boldsymbol{C}_{k,c}$ through singular value decomposition (SVD) [59].
7) Subtract $\boldsymbol{C}_{k,c}(0)$ from the original curve $\boldsymbol{C}_k$, rotate it using the rotation matrix $\boldsymbol{R}$, and add $\boldsymbol{C}_{k-1,c}(0)$ to obtain the final registered curve $\boldsymbol{C}_{k,reg}$.

The resulting curve $\boldsymbol{C}_{k,reg}$ is the registered curve at time step k with respect to the curve in the previous time step $\boldsymbol{C}_{k-1}$. Hence, the pose of the tip of $\boldsymbol{C}_{k,reg}$ is represented with respect to the reference frame of $\boldsymbol{C}_{k-1}$, which represents a relative pose relationship between consecutive time steps. To have a universal unchanging reference frame, instead of comparing time step k with time step $k-1$, it can be compared with time step $k=0$. This way, the pose of the instrument tip at any time step will be given with respect to the same reference frame of the curve in time step $k=0$.

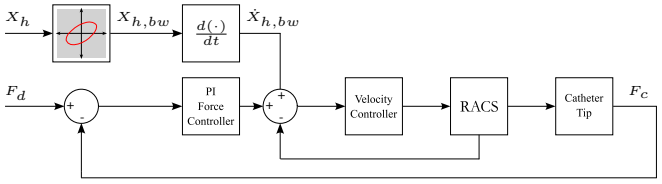

Fig. 7. Force controller block diagram. F_d and F_c are the desired and actual catheter tip contact forces, x_h is the estimated heart motion, $x_{h,bw}$ is the hysteresis compensated x_h, and $\dot{x}_{h,bw}$ is the temporal derivative of $x_{h,bw}$.

Figure 6D provides a comparison between the resulting instrument tip motion profile using EM reconstruction (considered as ground truth) and FBG-MCF reconstruction employing the aforementioned tip tracking strategy. The mean and maximum error between both motion profiles was found to be 0.16 ± 0.60 mm and 1.81 mm, respectively. The results, therefore, clearly illustrate the feasibility of the method and its applicability to instrument tip pose tracking and hysteresis identification applications.

V. Dynamic Tissue Contact Force Tracking

A. Contact Force Controller

The proposed contact force controller is shown in the block diagram of Fig. 7. The inner control loop is composed of a velocity controller that is fed with the estimated and hysteresis-compensated heart motion velocity $\dot{x}_{h,bw}$. A strategy based on a velocity controller was chosen to allow relative motion of the catheter tip rather than an absolute position-based motion which may include an undesirable constant offset. An outer force control loop with a standard PI controller is cascaded onto the velocity controller to maintain a constant tip contact force F_d equal to a desired force setpoint F_d.

B. Force Tracking Experiments

The experimental setup shown in Fig. 3E was again utilized for the force tracking experiments. A dynamic heart motion setup was added to mimic the real environment (see Fig. 3F). The setup was composed of a curved 3D-printed surface with a 2 mm thick Eco-Flex silicon layer. At its back end, a 6-axis force sensor was used to measure the contact force between the simulated heart tissue and the catheter tip. The simulated heart surface was attached to a linear servomotor and a linear guide to recreate a desired heart motion profile. The same heart motion profile as in Section IV.B was used for the force control experiments (see also Fig. 6C). Three force control strategies were implemented and compared. These are: ① PI force controller, ② the controller in ① combined with the estimated heart motion velocity as a feedforward to the velocity controller, and ③ the controller in ② but with Bouc-Wen hysteresis compensation of the feedforward signal. Note that the PI force controller was manually tuned to obtain the best force tracking performance. The PI gains were found to be $P=150\ \frac{mm}{sN}$ and $I=0\ \frac{mm}{s^2N}$, i.e. a purely proportional controller. For a contact force setpoint $F_d=0.2$ N, the force tracking results of the three force controllers are shown in

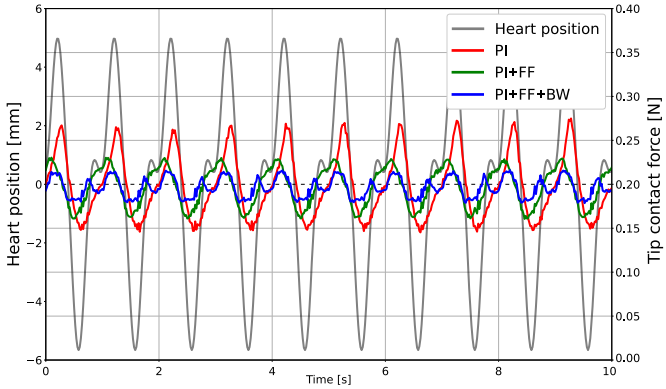

Fig. 8. Catheter contact force tracking results with a contact force setpoint of 0.2 N (PI = proportional and integral control, PI + FF = PI control combined with velocity feedforward, PI + FF + BW = PI control combined with velocity feedforward and Bouc-Wen hysteresis compensation).

Fig. 8. Force data was recorded for a period of 10 s for each experiment and repeated three times for each force control strategy. The mean and maximum force tracking errors were respectively: ① 0.0018 ± 0.0362 N and 0.0782 N (39.1% of setpoint), ② 0.0016 ± 0.0238 N and 0.0520 N (26.0%), and ③ 0.0020 ± 0.0119 N and 0.0253 N (12.7%). All force controllers maintained a contact force within the clinically predefined range of $0.1 - 0.4$ N. However, the performance of the force controller combined with feedforward and Bouc-Wen hysteresis compensation is clearly superior. This strategy can be useful in cases where the force range is even smaller and for more intricate contacts with delicate tissue.

VI. In-vivo Experimental Validation

A. Experimental Setup

Figure 9 illustrates the experimental scene in the animal CathLab. The RACS was mounted onto a multi-DoF jointed arm and attached onto the bedside rail. The RACS was then oriented towards the incision point within the swine. An incision was made into the right femoral artery of a 40 kg female swine. The CathLab was equipped with a mono-planer fluoroscopic C-arm and a dedicated display, as shown in Fig. 9A. The objective of the experiment was to prove the feasibility of employing the developed RACS to drive guidewires and catheters into a living animal from an incision point up to, and beyond, the heart region. Three types of data were recorded: *(1)* fluoroscopic images, *(2)* FBG-MCF wavelengths, and *(3)* RACS Hall sensor data. These three data types were recorded for the catheter specifically since the catheter had a MCF embedded within its irrigation channel. It was also necessary to evaluate the proposed tip pose tracking algorithm using FBG-MCF measurements. On the other hand, only fluoroscopic images were recorded for the guidewire since it was difficult to embed an MCF inside of it. Fluoroscopic images were used to visually prove the feasibility of driving both instruments into the vasculature using the RACS. The instruments were navigated from the incision point to the heart and backwards, through tele-operation using a joystick, for several times while continuously recording data.

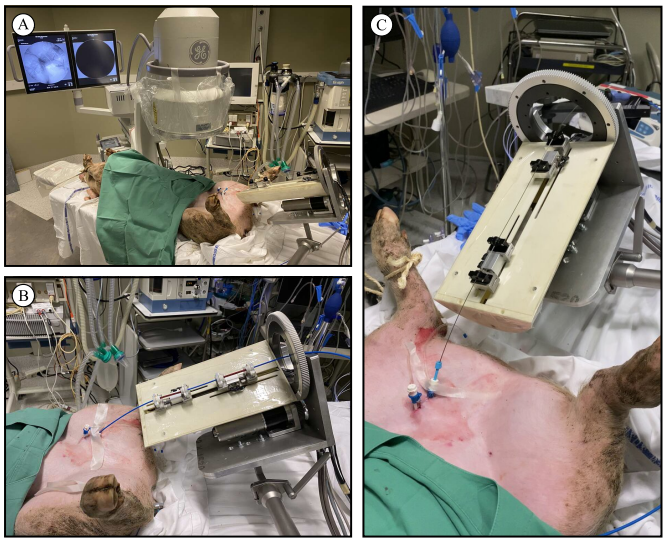

Fig. 9. Illustration of: Ⓐ the in-vivo experimental scene within the CathLab, and a close-up on the RACS with a deployed Ⓑ catheter and Ⓒ guidewire.

B. Experimental Results

Results of the in-vivo experiments demonstrated that the RACS was able to drive instruments smoothly through the vasculature towards the heart regions and beyond. Figure 10A shows a fluoroscopic image illustrating a guidewire driven passed the heart region towards the aortic arch. The RACS' sleeve-based grippers were able to overcome frictional forces throughout the motion within the vasculature. This was demonstrated for both instruments. To prove this quantitatively, data was recorded for the motion of the catheter from a starting initial point to a final end point, as shown in Fig. 10B. These two points were limited by the field-of-view of the fluoroscopic image to maintain visibility of the catheter tip. The method outlined in Section IV.C was used to determine the distance travelled by the catheter and to obtain the respective shape registration. Figures 10C and 10D illustrate an example result for this experiment. The distance travelled by the catheter is simply the shift in the curvature profile along its arc length. The initial and final shapes were registered and represented with respect to the same universal frame, as shown in Fig. 10D. The result clearly shows an overlap between the two shapes, supporting our previous assumption about the quasi-static shape of the surrounding sheath. The experiment was repeated three times in different locations. The distance travelled by the catheter was computed in two ways: *(1)* through the method outlined in Section IV.C, and *(2)* through the RACS' Hall sensor data. The mean absolute error between both measurements for all trials was 11.8 mm for a total distance travelled of around 135 mm. The discrepancy between both measurements can be attributed to the presence of hysteresis along the vasculature path and the coarse FBG spacing along the catheter, which was at every 10 mm intervals. Nonetheless, the distance travelled by the catheter can be improved by fusing both measurements to have a more precise estimation.

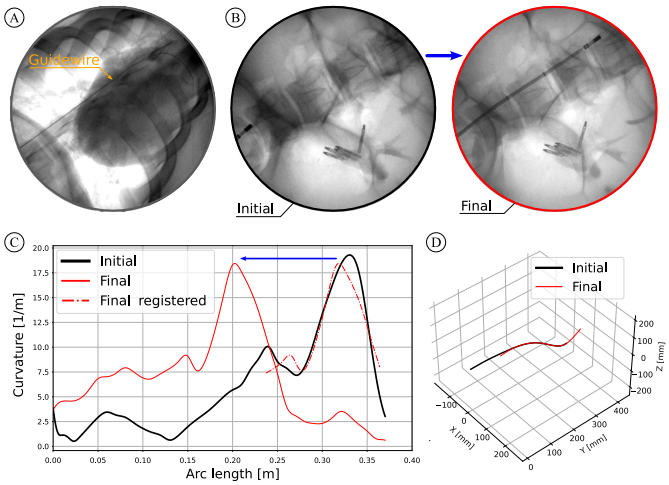

Fig. 10. Example result from the in-vivo experiments: Ⓐ guidewire driven by the RACS passed the heart towards the aortic arch, Ⓑ fluoroscopic image of the catheter at an initial position (left) and at a final position after its motion (right), Ⓒ catheter curvature profile at the initial and final positions, Ⓓ 3D catheter shape at the initial and final positions after registration.

VII. Discussion & Conclusion

This paper presented the development of a new RACS based on a braided sleeve gripper concept. The RACS was experimentally evaluated and characterized to validate its performance with respect to clinical requirements. The braided sleeve concept proved to be an adequate alternative to conventional driving mechanisms. The concept is simple, yet versatile in that it allows for easy instrument installation and continuous deployment. In principle, it can be easily made to conform to clinical sterility regulations. Furthermore, the RACS is able to achieve precise instrument tissue tracking. A new practical method based on FBG-inscribed MCFs was presented to achieve dynamic real-time instrument tip pose tracking within robotic catheterization procedures. This can be used for a myriad of applications including hysteresis identification and compensation, shape registration, and instrument travel distance estimation, as presented in this work. The RACS was also demonstrated to achieve high accuracy contact force tracking while maintaining the clinically predetermined force constraints. Furthermore, the RACS was evaluated within an in-vivo experimental environment on a live swine. The RACS successfully demonstrated its ability to drive instruments through the vasculature without complications or hindrances. The only observed limitation of the experimental setup was due to the large distance between the most distal RACS gripper and the insertion point of the sheath. The long and slender nature of the instruments caused buckling to occur in few occasions. This was mitigated during the experiments by manually guiding the instruments in that region. In principle, instrument buckling can be eliminated by simply minimizing the aforementioned distance, or by installing a dedicated piece to enclose the instrument in that region.

It is important to note that there are a few key aspects that have to be addressed in order to improve success chances for clinical translation. To begin with, an assembly has to be envisioned where two, or possibly more, RACS devices are configured and employed to drive guidewires and catheters simultaneously. In addition, a dedicated interface has to be developed to allow tele-operative control by an interventionalist. Moreover, the presented work in this paper evaluated various aspects such as hysteresis compensation, tissue motion tracking, and contact force tracking on a heart-resembling laboratory-based setup. While this is reasonably realistic and a good starting point to evaluate the methods and their feasibility, further experimentation has to be made on *(a)* real ex-vivo animal tissue, e.g. a porcine heart, and *(b)* within an in-vivo environment, i.e. one that is similar to what was described in this paper. The robustness and safety of the proposed estimation and force control methods must therefore be further validated within the scope of such intricate environments.

According to the above, future work will focus on RACS design optimizations focusing on modularity to drive multiple instruments simultaneously in addition to in-vivo validation of the proposed estimation and force control strategies.

Acknowledgments

The authors would like to thank the Flemish Agency of Innovation and Entrepreneurship (VLAIO) for funding this project (HBC.2018.2046).

References

[1] WHO, "World health statistics 2020: monitoring health for the SDGs, sustainable development goals, Geneva: World Health Organization, Tech. Rep. 1, 2020.

[2] A. Verma, *et al.*, "Approaches to Catheter Ablation for Persistent Atrial Fibrillation," *New England Journal of Medicine*, vol. 372, no. 19, pp. 1812–1822, 2015.

[3] X. Zhou, *et al.*, "Impact of contact force technology on reducing the recurrence and major complications of atrial fibrillation ablation: A systematic review and meta-analysis," *Anatolian Journal of Cardiology*, vol. 17, no. 2, pp. 82–91, 2017.

[4] K. Takashima, *et al.*, "Contact and friction between catheter and blood vessel," *Tribology International*, vol. 40, no. 2 SPEC. ISS., pp. 319–328, 2007.

[5] B. Schmidt, *et al.*, "Remote navigation systems in electrophysiology," *Europace*, vol. 10, no. Supplement 3, pp. 57–61, 2008.

[6] R. S. Wang and S. N. Ambani, "Robotic Surgery Training: Current Trends and Future Directions," pp. 137–146, 2021.

[7] K. C. K. Wong, *et al.*, "Mitral isthmus ablation is feasible, efficacious, and safe using a remote robotic catheter system," *PACE - Pacing and Clinical Electrophysiology*, vol. 36, no. 11, pp. 1364–1372, 2013.

[8] L. Cruddas, *et al.*, "Robotic endovascular surgery: current and future practice," *Seminars in Vascular Surgery*, vol. 34, no. 4, pp. 233–240, 2021.

[9] Y. Zhao, *et al.*, "Remote vascular interventional surgery robotics: A literature review," *Quantitative Imaging in Medicine and Surgery*, vol. 12, no. 4, 2022.

[10] C. B. Beaman, *et al.*, "A review of robotic interventional neuroradiology," pp. 808–814, 2021.

[11] J. Harrison, *et al.*, "Robotically-assisted percutaneous coronary intervention: Reasons for partial manual assistance or manual conversion," *Cardiovascular Revascularization Medicine*, vol. 19, no. 5, pp. 526–531, 2018.

[12] G. W. Britz, *et al.*, "Feasibility of Robotic-Assisted Neurovascular Interventions: Initial Experience in Flow Model and Porcine Model," *Clinical Neurosurgery*, vol. 86, no. 2, pp. 309–314, 2020.

[13] G. B. Bian, *et al.*, "An enhanced dual-finger robotic Hand for Catheter manipulating in vascular intervention: A preliminary study," in *2013 IEEE International Conference on Information and Automation, ICIA 2013*, 2013, pp. 356–361.

[14] T. Wang, *et al.*, "Remote-controlled vascular interventional surgery robot," *International Journal of Medical Robotics and Computer Assisted Surgery*, vol. 6, no. 2, pp. 194–201, 2010.

[15] N. Xiao, *et al.*, "A robotic catheter system with real-time force feedback and monitor," *Australasian Physical and Engineering Sciences in Medicine*, vol. 35, no. 3, pp. 283–289, 2012.

[16] Y. Fu, *et al.*, "The master-slave catheterisation system for positioning the steerable catheter," *International Journal of Mechatronics and Automation*, vol. 1, no. 3/4, p. 143, 2011.

[17] M. N. Faddis, *et al.*, "Novel, magnetically guided catheter for endocardial mapping and radiofrequency catheter ablation," *Circulation*, vol. 106, no. 23, pp. 2980–2985, 2002.

[18] X. Ma, *et al.*, "Evaluating performance of a novel developed robotic catheter manipulating system," *Journal of Micro-Bio Robotics*, vol. 8, no. 3-4, pp. 133–143, 2013.

[19] Y. Song, *et al.*, "Performance evaluation of a robot-assisted catheter operating system with haptic feedback," *Biomedical Microdevices*, vol. 20, no. 2, 2018.

[20] S. Guo, *et al.*, "A Novel Robot-Assisted Endovascular Catheterization System With Haptic Force Feedback," *IEEE Transactions on Robotics*, vol. 35, no. 3, pp. 685–696, 2019.

[21] L. Zhang, *et al.*, "Design and performance evaluation of collision protection-based safety operation for a haptic robot-assisted catheter operating system," *Biomedical Microdevices*, vol. 20, no. 2, 2018.

[22] O. M. Omisore, *et al.*, "Design of a Master-Slave Robotic System for Intravascular Catheterization during Cardiac Interventions," in *16th IEEE International Conference on Control, Automation, Robotics and Vision, ICARCV 2020*, 2020, pp. 996–1000.

[23] Y. Ganji, *et al.*, "Robot-assisted catheter manipulation for intracardiac navigation," *International Journal of Computer Assisted Radiology and Surgery*, vol. 4, no. 4, pp. 307–315, 2009.

[24] J. W. Park, *et al.*, "Development of a force-reflecting robotic platform for cardiac catheter navigation," *Artificial Organs*, vol. 34, no. 11, pp. 1034–1039, 2010.

[25] L. Cercenelli, *et al.*, "CathROB: A Highly Compact and Versatile Remote Catheter Navigation System," *Applied Bionics and Biomechanics*, vol. 2017, 2017.

[26] S. Norouzi-Ghazbi, *et al.*, "Design and experimental evaluation of an automated catheter operating system," *Artificial Organs*, vol. 45, no. 6, pp. E171–E186, 2021.

[27] X. Wang, *et al.*, "Experimental validation of robot-assisted cardiovascular catheterization: model-based versus model-free control," *International Journal of Computer Assisted Radiology and Surgery*, vol. 13, no. 6, pp. 797–804, 2018.

[28] K. H. Lee, *et al.*, "MR Safe Robotic Manipulator for MRI-Guided Intracardiac Catheterization," *IEEE/ASME Transactions on Mechatronics*, vol. 23, no. 2, pp. 586–595, 2018.

[29] Z. Dong, *et al.*, "High-Performance Continuous Hydraulic Motor for MR Safe Robotic Teleoperation," *IEEE Robotics and Automation Letters*, vol. 4, no. 2, pp. 1964–1971, 2019.

[30] X. Bao, *et al.*, "Design and evaluation of sensorized robot for minimally vascular interventional surgery," *Microsystem Technologies*, vol. 25, no. 7, pp. 2759–2766, 2019.

[31] X. Bao, *et al.*, "Multilevel Operation Strategy of a Vascular Interventional Robot System for Surgical Safety in Teleoperation," *IEEE Transactions on Robotics*, vol. 38, no. 4, pp. 2238–2250, 2022.

[32] Y. Xiang, *et al.*, "Master-Slave Guidewire and Catheter Robotic System for Cardiovascular Intervention," in *2019 28th IEEE International Conference on Robot and Human Interactive Communication, RO-MAN 2019*, 2019.

[33] M. E. Abdelaziz, *et al.*, "Toward a Versatile Robotic Platform for Fluoroscopy and MRI-Guided Endovascular Interventions: A Pre-Clinical Study," in *IEEE International Conference on Intelligent Robots and Systems*, 2019, pp. 5411–5418.

[34] K. Wang, *et al.*, "Design and Performance Evaluation of Real-time Endovascular Interventional Surgical Robotic System with High Accuracy," *International Journal of Medical Robotics and Computer Assisted Surgery*, vol. 14, no. 5, 2018.

[35] Q. Lu, *et al.*, "A Novel Universal Endovascular Robot for Peripheral Arterial Stent–Assisted Angioplasty: Initial Experimental Results," *Vascular and Endovascular Surgery*, vol. 54, no. 7, pp. 598–604, 2020.

[36] G. Srimathveeravalli, *et al.*, "Design and fabrication of a robotic mechanism for remote steering and positioning of interventional devices," *International Journal of Medical Robotics and Computer Assisted Surgery*, vol. 6, no. 2, pp. 160–170, 2010.

[37] O. Al-Ahmad, *et al.*, "Local One-Dimensional Motion Estimation Using FBG-Based Shape Sensing for Cardiac Applications," *IEEE Robotics and Automation Letters*, vol. 7, no. 3, pp. 8122–8129, jul 2022.

[38] Y. Thakur, *et al.*, "Characterization of catheter dynamics during percutaneous transluminal catheter procedures," *IEEE Transactions on Biomedical Engineering*, vol. 56, no. 8, pp. 2140–2143, 2009.

[39] H. Rafii-Tari, *et al.*, "Assessment of navigation cues with proximal force sensing during endovascular catheterization," in *Lecture Notes in Computer Science (including subseries Lecture Notes in Artificial Intelligence and Lecture Notes in Bioinformatics)*, vol. 7511 LNCS, no. Pt 2, 2012, pp. 560–567.

[40] H. Rafii-Tari, *et al.*, "Objective Assessment of Endovascular Navigation Skills with Force Sensing," *Annals of Biomedical Engineering*, vol. 45, no. 5, pp. 1315–1327, 2017.

[41] H. Lee, *et al.*, "Design and control of a robotic steering mechanism for electrophysiological catheters," *Journal of Mechanisms and Robotics*, vol. 13, no. 1, 2021.

[42] S. Hasanzadeh, *et al.*, "Backlash characterization and position control of a robotic catheter manipulator using experimentally-based kinematic model," *Mechatronics*, vol. 44, pp. 94–106, 2017.

[43] O. M. Omisore, *et al.*, "Towards Characterization and Adaptive Compensation of Backlash in a Novel Robotic Catheter System for Cardiovascular Interventions," 2018.

[44] S. B. Kesner and R. D. Howe, "Position control of motion compensation cardiac catheters," *IEEE Transactions on Robotics*, vol. 27, no. 6, pp. 1045–1055, 2011.

[45] P. M. Loschak, *et al.*, "Automatically steering cardiac catheters in vivo with respiratory motion compensation," *International Journal of Robotics Research*, vol. 39, no. 5, pp. 586–597, 2020.

[46] X. Yu, *et al.*, "Adaptive-Constrained Impedance Control for Human-Robot Co-Transportation," *IEEE Transactions on Cybernetics*, vol. 52, no. 12, pp. 13 237–13 249, dec 2021. [Online]. Available: https://ieeexplore.ieee.org/document/9548781/

[47] X. Zhang, *et al.*, "Robotic Actuation and Control of a Catheter for Structural Intervention Cardiology," in *2022 IEEE/RSJ International Conference on Intelligent Robots and Systems (IROS)*. IEEE, oct 2022, pp. 5907–5913. [Online]. Available: https://ieeexplore.ieee.org/document/9981676/

[48] D. Wu, *et al.*, "Deep-Learning-Based Compliant Motion Control of a Pneumatically-Driven Robotic Catheter," *IEEE Robotics and Automation Letters*, vol. 7, no. 4, pp. 8853–8860, oct 2022. [Online]. Available: https://ieeexplore.ieee.org/document/9807375/

[49] H. Ma, *et al.*, "Dynamic coronary roadmapping via catheter tip tracking in X-ray fluoroscopy with deep learning based Bayesian filtering," *Medical Image Analysis*, vol. 61, 2020.

[50] N. Ouzir, *et al.*, "Robust Cardiac Motion Estimation with Dictionary Learning and Temporal Regularization for Ultrasound Imaging," in *IEEE International Ultrasonics Symposium, IUS*, vol. 2019-Octob, 2019, pp. 2326–2329.

[51] G. S. Fung, *et al.*, "Motion estimation for cardiac functional analysis using two x-ray computed tomography scans:," *Medical Physics*, vol. 44, no. 9, pp. 4677–4686, 2017.

[52] G. Fagogenis, *et al.*, "Autonomous robotic intracardiac catheter navigation using haptic vision," *Science Robotics*, vol. 4, no. 29, 2019.

[53] C. V. Graves, *et al.*, "Cardiac motion estimation using pyramid, warping, and cost volume neural network," in *SPIE 11600, Medical Imaging 2021*, 2021, p. 30.

[54] J. P. Moore and M. D. Rogge, "Shape sensing using multi-core fiber optic cable and parametric curve solutions," *Optics Express*, vol. 20, no. 3, pp. 2967–2973, 2012.

[55] O. Al-Ahmad, *et al.*, "Improved FBG-Based Shape Sensing Methods for Vascular Catheterization Treatment," *IEEE Robotics and Automation Letters*, vol. 5, no. 3, pp. 4687–4694, 2020.

[56] M. Rakotondrabe, "Bouc-Wen modeling and inverse multiplicative structure to compensate hysteresis nonlinearity in piezoelectric actuators," *IEEE Transactions on Automation Science and Engineering*, vol. 8, no. 2, pp. 428–431, 2011.

[57] T. N. Do, *et al.*, "Hysteresis modeling and position control of tendon-sheath mechanism in flexible endoscopic systems," *Mechatronics*, vol. 24, no. 1, pp. 12–22, 2014.

[58] S. G. Yuen, *et al.*, "Robotic motion compensation for beating heart intracardiac surgery," *International Journal of Robotics Research*, vol. 28, no. 10, pp. 1355–1372, 2009.

[59] S. Oomori, *et al.*, "Point cloud matching using singular value decomposition," *Artificial Life and Robotics*, vol. 21, no. 2, pp. 149–154, 2016.